*Article*

Porous SiO₂ Encapsulation for Selective Suppression of Hydrogen Evolution in Photocatalytic CO₂ Reduction

Junhao Lu [1], Yanan Li [1,2,3], Yiduo Wang [1], Qingqing Guan [1], Zixing Ge [1,2,3], Yuan Ren [1,2,3], Yaohui Zhao [1,2,3], Qian Wang [1], and Mingshang Jin [1,2,3,*]

1   State Key Laboratory of Multiphase Flow in Power Engineering, Xi'an Jiaotong University, Xi'an 710049, China
2   Frontier Institute of Science and Technology, Xi'an Jiaotong University, Xi'an 710049, China
3   Interdisciplinary Research Center of Frontier Science and Technology, Xi'an Jiaotong University, Xi'an 710049, China
*   Correspondence: jinm@mail.xjtu.edu.cn

Abstract: Photocatalytic carbon dioxide reduction reaction (CO₂RR) represents a promising route for sustainable energy conversion. However, in conventional solid-liquid-gas reaction systems, inefficient CO₂ diffusion to the catalyst surface often leads to dominant hydrogen evolution reaction (HER), limiting CO₂ conversion efficiency and product selectivity. Herein, we propose a catalyst encapsulation strategy using porous silicon dioxide (SiO₂) to spatially control molecular transport toward the active sites. By encapsulating Ag-modified titanium dioxide within a porous SiO₂ layer, we effectively restrict water access to the catalytic interface while facilitating CO₂ permeation. As a result, the parasitic HER is significantly suppressed, enabling an exceptional 100% selectivity for CO production from photocatalytic CO₂ reduction in pure water, which is a dramatic improvement from the mere 5.9% CO selectivity of the unencapsulated Ag-TiO₂ catalyst. This design achieves near-complete suppression of HER and 100% selectivity toward CO production under photocatalytic conditions. Our work provides a versatile interfacial engineering approach to overcome mass transfer limitations in three-phase photocatalytic systems, opening avenues for efficient gas-involving photoreactions.
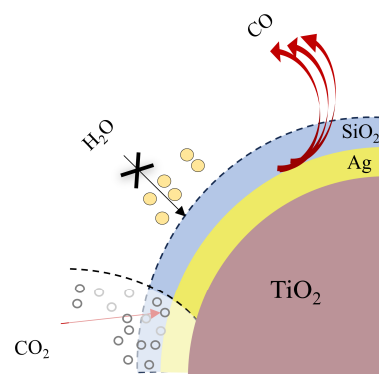
Keywords: CO₂RR; SiO₂ shell; core-shell; HER suppression; interface engineering

1. Introduction

With the rapid development of industry and economy globally, the massive consumption of finite fossil fuels has led to severe environmental issues, notably the greenhouse effect driven by rising atmospheric CO₂ levels [1–4]. In this context, photocatalytic CO₂ reduction reaction (CO₂RR) stands out as a promising strategy for converting solar energy into sustainable fuels, often regarded as the "holy grail" of energy conversion [5–8]. From the perspectives of sustainability and environmental friendliness, using water as the hydrogen source for CO₂RR is highly desirable [9,10]. However, a significant challenge persists in aqueous-phase photocatalytic CO₂RR, which is the severe competition from the hydrogen evolution reaction (HER) [11,12]. In typical aqueous reaction systems, HER tends to dominate over CO₂RR, primarily due to the kinetically more favorable proton reduction pathway. This fierce competition results in unsatisfactory selectivity for carbon-based products and low CO₂RR efficiency in most cases [13,14].

Although substantial efforts have been devoted to enhancing CO₂RR performance through catalyst design, such as developing novel semiconductors, morphology control, doping, and constructing heterojunctions [5,15–19], these strategies often focus on modifying the intrinsic electronic structure of the catalysts. For instance, Sun et al. designed an N, S-codoped Fe-based MIL-88B catalyst with a well-defined bipyramidal hexagonal prism morphology, achieving a high C₂H₄ yield of 17.7 μmol g⁻¹ h⁻¹ [20]. Meanwhile, Wang et al. anchored Ag single atoms on hollow porous polygonal C₃N₄ nanotubes to form a photocatalyst, showing up to 94% CO selectivity [21]. Despite these advances, effectively suppressing the competing HER to achieve near-unity product selectivity remains a critical and unresolved issue.

Recent studies have highlighted that the interfacial microenvironment of the catalyst plays a decisive role in governing the reaction pathway [22]. The simultaneous presence of water molecules and CO_2 reactants at the catalyst surface creates a direct competition between HER and CO_2RR [23]. Therefore, precisely controlling the transport of key molecules (H_2O and CO_2) to the active sites is crucial for steering the selectivity. Conventional approaches, such as employing organic hole scavengers, can alter the reaction microenvironment but introduce problems like high cost, toxicity, and compromised sustainability [24,25].

To address the fundamental challenge of HER dominance, we propose an interfacial engineering strategy centered on selectively inhibiting the access of water to the catalytic active sites. Herein, we demonstrate a porous silicon dioxide (SiO_2) encapsulation layer coated on Ag-loaded TiO_2 photocatalysts (Ag-TiO_2@SiO_2). This design does not aim to enhance CO_2 diffusion but rather to create a localized hydrophobic microenvironment that preferentially restricts the migration of water molecules to the reaction interface while allowing CO_2 permeation. As a result, the parasitic HER is significantly suppressed, enabling an exceptional 100% selectivity for CO production from photocatalytic CO_2 reduction in pure water, which is a dramatic improvement from the mere 5.9% CO selectivity of the unencapsulated Ag-TiO_2 catalyst. This work provides a distinct and effective solution to the selectivity challenge by managing the interfacial reactant supply, opening new avenues for optimizing various multiphase photocatalytic processes.

2. Experimental Section

2.1. Materials and Methods

All chemicals were of analytical grade and used without further. TiO_2 nanoparticles (P25, Degussa, Germany) were used as the photocatalyst. $AgNO_3$ (99.8%), acetone (99.9%), ethanol (95%), tetraethyl orthosilicate (TEOS) and ammonia aqueous solution (28%) were purchased from Sinopharm Chemical Reagent Co. (Shanghai, China). Hexadecyl trimethyl ammonium Bromide (CTAB) was purchased from Shanghai Aladdin Biochemical Technology Co. (Shanghai, China). Deionized water (H_2O, 18.25 MΩ·cm) supplied by an UP-Water Purification System was used in the whole experimental process.

2.1.1. Synthesis of Ag-TiO_2

Ag nanoparticles were loaded onto the surface of TiO_2 to form Ag-TiO_2 nanoparticles using a photo-loading method. Water, methanol, and $AgNO_3$ were used as solvent, holes sacrificial agent, and Ag source, respectively. For the preparation of Ag-TiO_2, 0.2 g TiO_2 was dispersed in an aqueous solution containing 40 mL H_2O and 10 mL ethanol under sonication. Then, 0.5 mL $AgNO_3$ aqueous solution (50 mM) was added with vigorous stirring and continuously bubbled using high purity Ar gas for 30 min. Subsequently, the mixture was moved to a sealed transparent container and irradiated under a 300 W xenon lamp (Beijing China Education Au-light Co., Ltd. CEL-HXF300-T3) for 60 min. The as-prepared Ag-TiO_2 nanoparticles were separated by centrifugation and washed three times with water, and dried at 60 °C overnight.

2.1.2. Synthesis of Ag-TiO_2@SiO_2

The Ag-TiO_2@SiO_2 particles were prepared according to Stöber method. In a typical procedure, 100 mg Ag-TiO_2 and 300 mg CTAB were dispersed in the mixture of ethanol (80 mL) and water (20 mL) and 1 mL of ammonia aqueous solution (28 wt%) under stirring for 30 min, then 200 μL of TEOS was added slowly with continuous stirring for 2 h. The particles were collected by centrifugation and washed with ethanol and water, respectively. The CTAB surfactant was removed by solvent extraction method using 120 mL of acetone solution and refluxed at 80 °C for 48 h. This extraction process was repeated three times. After centrifugating and washing with ethanol and water, the Ag-TiO_2@SiO_2-2 core-shell nanocarriers were obtained. By altering the amount of TEOS to 50 μL or 400 μL, Ag-TiO_2@SiO_2-1 and Ag-TiO_2@SiO_2-3 were obtained. Ag-TiO_2@SiO_2-2 is commonly abbreviated as Ag-TiO_2@SiO_2.

2.1.3. Synthesis of Ag-TiO_2@D-SiO_2

In a typical procedure, 100 mg Ag-TiO_2 were dispersed in the mixture of ethanol (80 mL) and water (20 mL) and 1 mL of ammonia aqueous solution (28 wt%) under stirring for 30 min, then 200 μL of TEOS was added slowly with continuous stirring for 2 h. The particles were collected by centrifugation and washed with ethanol and water, the Ag-TiO_2@D-SiO_2 core-shell nanocarriers were obtained.

2.1.4. Synthesis of SiO_2

In a typical procedure, 300 mg CTAB were dispersed in the mixture of ethanol (80 mL) and water (20 mL) and 1 mL of ammonia aqueous solution (28 wt%) under stirring for 30 min, then 200 μL of TEOS was added slowly with continuous stirring for 2 h. The particles were collected by centrifugation and washed with ethanol and water, respectively.

2.1.5. Synthesis of Ag-TiO_2-CTAB

In a typical procedure, 100 mg Ag-TiO_2 and 300 mg CTAB were dispersed in the mixture of ethanol (80 mL) and water (20 mL) and 1 mL of ammonia aqueous solution (28 wt%) under stirring for 2 h, The particles were collected by centrifugation and washed with ethanol and water, respectively.

2.1.6. Synthesis of Ag-TiO_2@SiO_2-NaOH

Ag-TiO_2@SiO_2-NaOH were prepared by etching Ag-TiO_2@SiO_2 in 10 mL of 2 M NaOH solution at 80 °C for 1 h.

2.2. Characterization

High-resolution TEM (HRTEM) images, high-angle annular dark-field scanning transmission microscopy (HAADF-STEM) images, and energy-dispersive X-ray spectroscopy (EDS) elemental mappings and line scans were performed on a JEM-F200 microscope equipped with a built-in EDS operated at 200 kV. The powder X-ray diffraction (PXRD) patterns were obtained on a Rigaku SmartLab, using Cu Kα (λ = 0.15406 nm) radiation. Textural properties of the catalysts were measured by N_2 physisorption at -196 °C on Micromeritics ASAP 2460 instrument. X-ray photoelectron spectroscopy (XPS) was conducted using a Thermo Fisher ESCALAB Xi+ spectrometer equipped with monochromatic Al Kα radiations. The Ag 3d, Ti 2p, O 1s and Si 2p peaks, as well as the valence bands, were corrected using the C 1s contamination peak (284.8 eV) as a reference. The content of Ag of the samples were determined by inductively coupled plasma mass spectrometry (ICP-MS), using a PerkinElmer NexION 350D (Waltham, MA, USA). Water-droplet contact angle tests were performed on the JY-82B contact angle goniometer. An Intrinsic DVS instrument from Surface Measurement Systems was used to perform the water vapor adsorption and desorption experiments over a humidity range of 0 ~ 95%. Each humidity step was made if less than a 0.002% weight change occurred over 10 min, with a maximum hold time of 240 min.

2.3. Photocatalytic CO_2RR Measurements

The photocatalytic CO_2 reduction measurements were carried out in a sealed reaction system. A 300 W Xe lamp (Beijing China Education Au-light Co., Ltd. CEL-HXF300-T3) was used as the light source providing a full spectrum illumination. In the photocatalytic process, 5 mg catalyst powder and 20 mL water were placed in a quartz reactor with a window area of 16 cm^2 and a volume of 130 mL. Before reaction, the reactor was purged with high purity CO_2 (99.999%) for 30 min. During the reaction, the reactor was placed on a magnetic stirrer, and the stirring speed was set at 800 rpm. The reaction temperature is controlled at 25 °C with a water circulator. Reaction was stopped after 4 h. The gas products were quantitatively analyzed by a gas chromatograph (SHIMANZU GC-2014) equipped with flame ionization detector (FID) and thermal conductivity detector (TCD).

The isotope-labeling experiments were carried out under the same experimental conditions, except that $^{12}CO_2$ was replaced with $^{13}CO_2$. The ^{13}C-labeled products were analyzed using a gas chromatograph-mass spectrometer (GC-MS, Agilent 5977B GC/MSD). In cycling measurements, the catalyst was washed with ultrapure water to remove surface adsorbates before each reaction cycle. In this work the selectivity of catalyst for CO_2 reduction to acetate was calculated by following equation:

$$Selectivity~(\%) = n(CO)/[n(H_2) + n(CO) + n(CH_4) + n(C_2H_4)] \times 100\%$$

where, $n(H_2)$, $n(CO)$, $n(CH_4)$ and $n(C_2H_4)$ are the mole amounts of produced H_2, CO, CH_4 and C_2H_4, respectively.

3. Results and Discussion

The core-shell structured Ag-TiO_2@SiO_2 photocatalyst was synthesized via a two-step procedure, as illustrated in Figure 1a. Initially, Ag nanoparticles were deposited on the surface of TiO_2 through a photo-deposition process to form Ag-TiO_2 nanoparticles (Figure S1) [26]. Subsequently, a porous SiO_2 shell was encapsulated onto the Ag-TiO_2 nanoparticles using the Stöber method [27]. This rational design aims to selectively control the transport of reactant molecules (H_2O and CO_2) to the active sites by creating a physical barrier, thereby

addressing the critical issue of HER competing with CO_2RR in the three-phase photocatalytic system. The X-ray diffraction (XRD) patterns (Figure 1b) of both Ag-TiO_2 and Ag-TiO_2@SiO_2 are identical to that of the pristine TiO_2, showing a mixed phase of anatase and rutile. The absence of distinct Ag diffraction peaks is attributed to its low loading and high dispersion [28]. Transmission electron microscopy (TEM) images (Figure 1c) confirmed the successful encapsulation of Ag-TiO_2 nanoparticles by a uniform SiO_2 shell, typically 5-15 nm thick. High-resolution TEM (HRTEM) analysis (Figures 1d and S2) reveals lattice fringes of 0.352 nm and 0.236 nm, corresponding to the (101) plane of anatase TiO_2 and (111) plane of metallic Ag, respectively. Energy-dispersive X-ray spectroscopy (EDS) mapping (Figure 1e) further verifies the core-shell structure, showing a homogeneous distribution of Ag, Ti, and O elements in the core, while the Si signal forms a distinct shell surrounding the core.
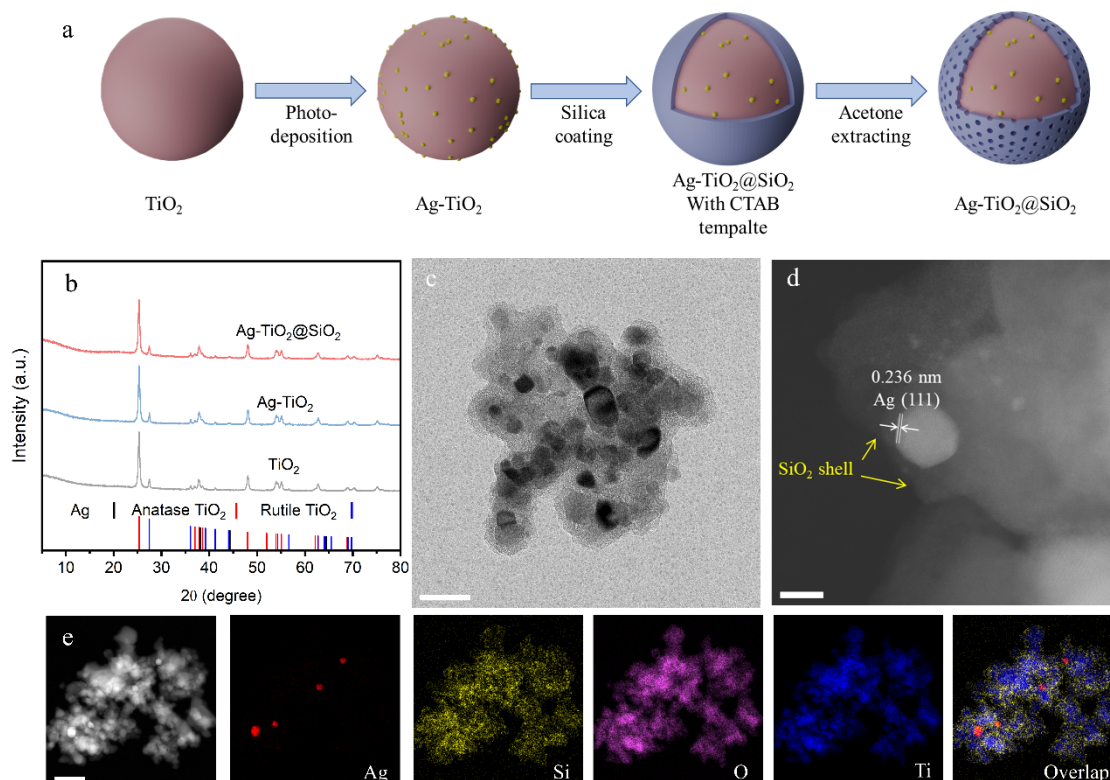

Figure 1. (**a**) Schematic illustration of the formation of Ag-TiO_2@SiO_2. (**b**) XRD patterns of TiO_2, Ag-TiO_2 and Ag-TiO_2@SiO_2. (**c**)TEM image of Ag-TiO_2@SiO_2, scale bars: 50 nm. (**d**) HRTEM image of Ag-TiO_2@SiO_2, scale bars: 5 nm. (**e**) STEM image of Ag-TiO_2@SiO_2 and corresponding element mapping (Ag, Si, O, and Ti), scale bars: 100 nm.

The chemical structures of the Ag-TiO_2 and Ag-TiO_2@SiO_2 nanoparticles were further examined by Fourier transform infrared (FTIR) spectroscopy. As shown in Figure 2a, the FTIR spectra offer clear evidence of functional groups and chemical bonds present in both samples. In each spectrum, the peak at 409 cm^{-1} is associated with the Ti-O-Ti vibration of the TiO_2 crystal framework, confirming its presence as the primary component [29]. Additional peaks at 3445 cm^{-1} and 1632 cm^{-1} correspond to the O-H stretching and bending vibrations, respectively, indicating the presence of adsorbed water molecules on the nanoparticle surfaces. Notably, the Ag-TiO_2@SiO_2 sample exhibits a distinct peak at 1072 cm^{-1}, which is characteristic of the asymmetric stretching vibration of Si-O-Si bonds, confirming the successful formation of a SiO_2 shell. Also observable in the Ag-TiO_2@SiO_2 spectrum are several peaks associated with the structure-directing agent CTAB, including the C-N stretching vibration at 1481 cm^{-1} and the $-CH_2-$ rocking vibrations at 2922 cm^{-1} and 2852 cm^{-1} [27]. The presence of these organic residues suggests that CTAB is incorporated into the SiO_2 shell, which likely influences the material's final porosity and surface properties, which is crucial for forming the porous and hydrophobic shell.

X-ray photoelectron spectroscopy (XPS) was further conducted to probe the surface chemical states and elemental composition of Ag-TiO_2 and Ag-TiO_2@SiO_2 nanoparticles. As illustrated in Figure 2b, the XPS survey spectrum of Ag-TiO_2 exhibits distinct photoelectron peaks corresponding to Ag and Ti, indicating the presence of both metallic Ag and TiO_2 on the surface. In contrast, the survey spectrum of Ag-TiO_2@SiO_2 shows a substantial attenuation of the Ag and Ti signals, while new and prominent peaks corresponding to Si are observed (Figure S3). This marked decrease in signal intensity from the underlying Ag-TiO_2 core, coupled with the emergence of Si-related peaks, provides strong evidence

for the formation of a continuous and conformal SiO_2 shell layer coating the surface, which effectively shields the photoelectrons emitted from the core material, which is consistent with the TEM observations.
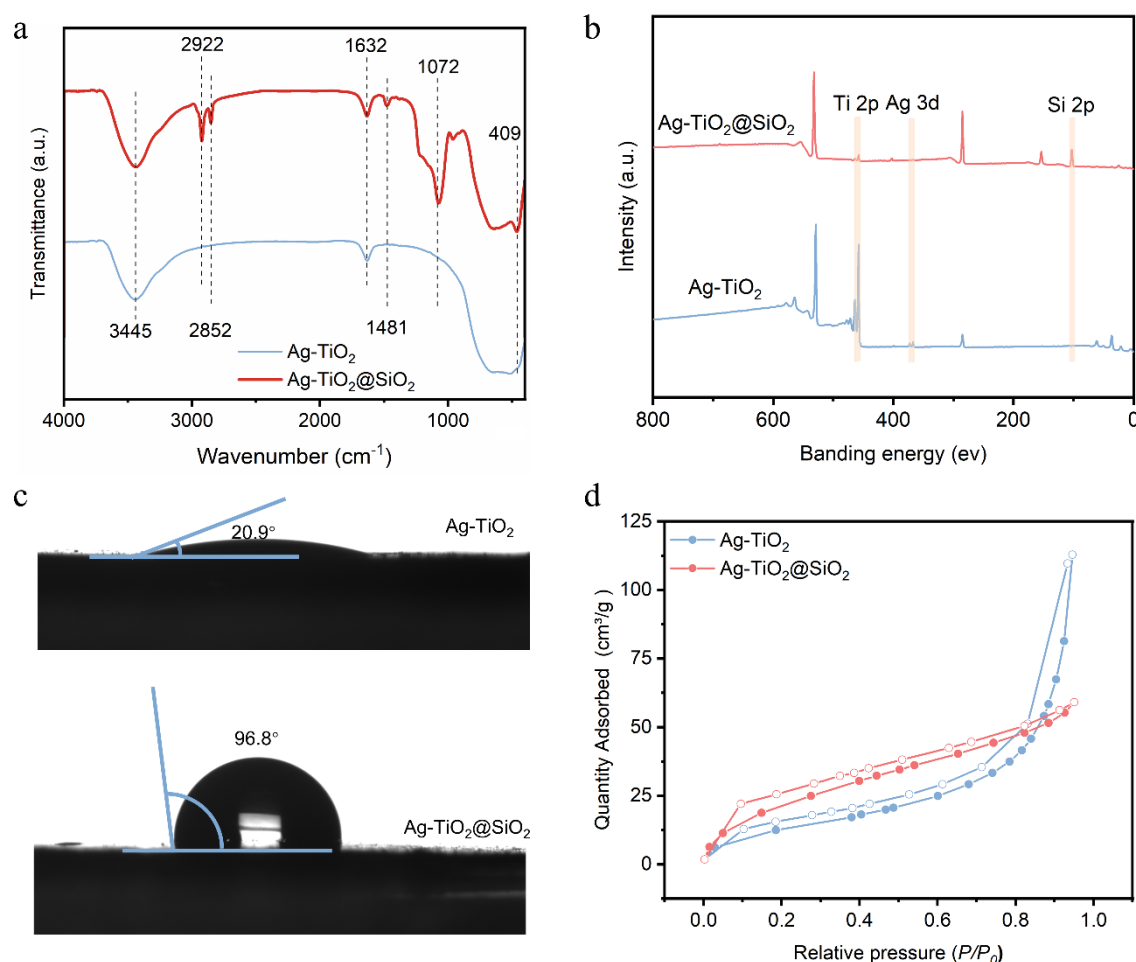

Figure 2. (**a**) FTIR spectra of Ag-TiO_2 and Ag-TiO_2@SiO_2, (**b**) XPS spectra of Ag-TiO_2 and Ag-TiO_2@SiO_2. (**c**) Water-droplet contact angle tests. (**d**) The water vapor adsorption and desorption tests of Ag-TiO_2 and Ag-TiO_2@SiO_2.

To validate the role of the SiO_2 shell in modulating the interfacial microenvironment, we systematically characterized the surface physicochemical properties. Water contact angle measurements (Figure 2c) revealed that the pristine Ag-TiO_2 surface is hydrophilic (contact angle of 20.9°). In stark contrast, the Ag-TiO_2@SiO_2 surface exhibited a significantly increased contact angle of 96.8°, demonstrating that the SiO_2 coating effectively enhanced surface hydrophobicity. This property is pivotal for inhibiting the migration of water molecules to the active interface. Specific surface area and pore size distribution analyses (Figure S4) indicated that Ag-TiO_2 and Ag-TiO_2@SiO_2 possess comparable specific surface areas. However, notable differences were observed in their pore size distributions. Ag-TiO_2 exhibited a broad distribution of micropores, mesopores, and macropores. In contrast, Ag-TiO_2@SiO_2 showed a relatively narrower distribution, primarily centered on micropores and small mesopores with a pronounced peak at 3.6 nm, which is characteristic of the mesopores within the SiO_2 shell. This tailored porosity is expected to facilitate the diffusion of CO_2 gas while imposing mass transfer resistance for water molecules. The isothermal water adsorption curves (Figure 2d) strongly support this inference that Ag-TiO_2@SiO_2 exhibited inferior water adsorption capacity, especially in the high relative pressure region, compared to Ag-TiO_2. This can be directly attributed to its hydrophobic surface and mesoporous-dominated structure, which collectively suppress water accumulation on the catalyst surface.

Based on the structural characterization, the photocatalytic CO_2 reduction performance of the as-prepared samples was systematically evaluated in aqueous medium without any sacrificial agent. The reactions were carried out under irradiation from a 300 W xenon lamp, and the gas products were quantified using gas chromatography (GC). As shown in Figure 3a, no reaction products were detected for the exposed SiO_2 nanoparticles (Figure S5), owing to their inherent insulating properties, the unmodified Ag-TiO_2 exhibited strong hydrogen evolution activity with only 5.9% selectivity toward CO, while producing minor amounts of CH_4 and C_2H_4, consistent with its hydrophilic surface property that favors water adsorption and proton reduction. In contrast, after encapsulation

with a porous SiO_2 shell, Ag-TiO_2@SiO_2 achieved 100% selectivity for CO, with H_2 evolution being completely suppressed. The hydrophobic micropores within the CTAB-templated SiO_2 shell create a locally hydrogen-deficient environment, which significantly lowers the surface concentration of reactive H species. As a result, the CO* intermediate formed on the Ag-TiO_2 surface is also prevented from undergoing further hydrogenation to CH_4 or C-C coupling to C_2H_4, and instead desorbs as CO. Although the CO evolution rate over Ag-TiO_2@SiO_2 (6.20 $\mu mol \cdot g^{-1} \cdot h^{-1}$) did not increase significantly compared to that of Ag-TiO_2. To decouple the mechanistic contributions of the SiO_2 shell from residual CTAB, we synthesized two reference materials: Ag-TiO_2@D-SiO_2 (CTAB-free with a dense SiO_2 shell) and Ag-TiO_2-CTAB (SiO_2-free with only surface-adsorbed CTAB). Performance testing revealed that while Ag-TiO_2-CTAB, lacking the SiO_2 shell, achieved 53.6% CO selectivity, this remained substantially lower than Ag-TiO_2@SiO_2. Conversely, Ag-TiO_2@D-SiO_2 without CTAB exhibited 100% CO selectivity but demonstrated a markedly reduced CO desorption rate (3.00 $\mu mol \cdot g^{-1} \cdot h^{-1}$), primarily due to a significant decrease in specific surface area. To further confirm the origin of hydrophobicity, we removed the SiO_2 shell by NaOH etching. After etching, the CO selectivity of the catalyst dropped to 23% (Figure S6), providing additional evidence that the SiO_2 shell is crucial for inhibiting HER. These findings confirm that the SiO_2 shell serves as the primary barrier against HER, the core function of the porous SiO_2 shell is not to enhance intrinsic activity, but rather to precisely inhibit the hydrocracking pathway by constructing a hydrophobic interfacial microenvironment. This strategic regulation directs the reaction towards near-perfect carbon dioxide reduction selectivity. On the other hand, the SiO_2 shell thickness is another critical parameter influencing catalytic performance. By varying the amount of TEOS added during synthesis, we prepared Ag-TiO_2@SiO_2 samples with different shell thicknesses. Performance evaluation revealed that an excessively thin shell still allows water molecules to reach the reaction interface, resulting in lower CO selectivity. Conversely, an overly thick SiO_2 shell reduces the proportion of active catalytic components in the material, thereby diminishing overall photocatalytic activity. Therefore, rational control of the SiO_2 shell thickness is essential (Figure S7). Inductively coupled plasma (ICP) analysis conducted before and after the 4-h photocatalytic reaction revealed negligible Ag leaching, with a quantified Ag loss of only ~0.16 wt%, thereby confirming the excellent structural stability and retention capability of Ag species in the catalyst under operational conditions (Table S3). The cycling test (Figure 3c) further demonstrated the excellent photocatalytic stability of Ag-TiO_2@SiO_2 over five consecutive runs, confirming the robustness of the core-shell structure [30]. Control experiments (Figure 3d) verified that no CO was detected in the absence of CO_2, light irradiation, or photocatalyst, indicating that the reaction is truly photocatalytic and dependent on all three components. Moreover, isotope labeling experiments using $^{13}CO_2$ (Figure 3e) clearly demonstrated that the produced CO originated from the supplied CO_2, ruling out contributions from carbonaceous impurities [31].
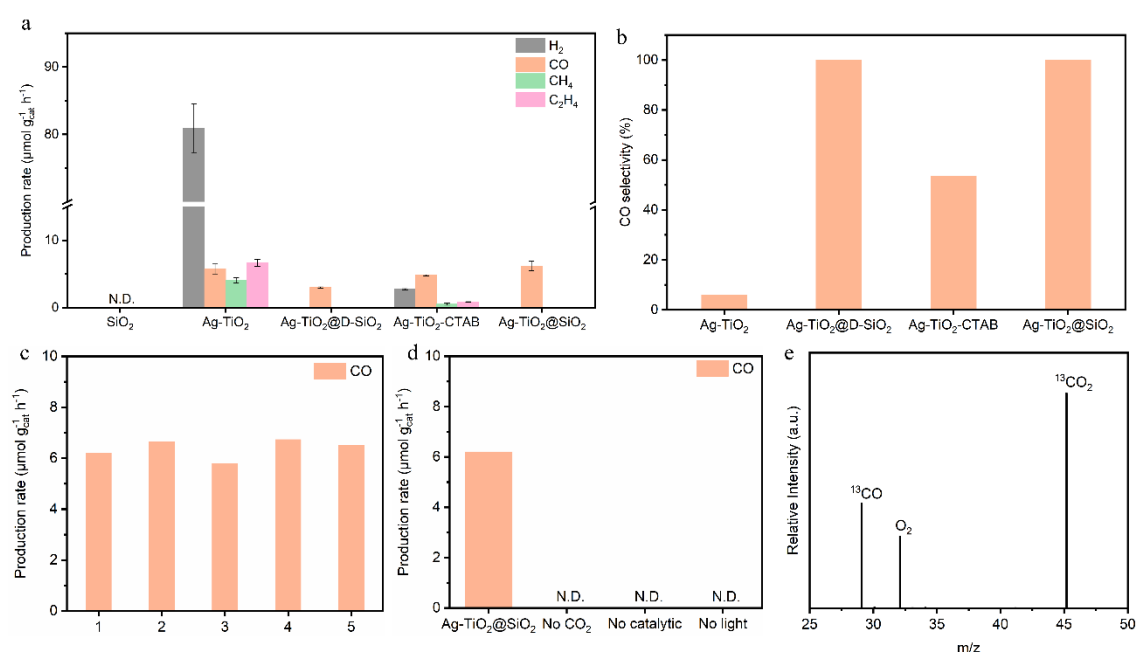

Figure 3. (a) The photocatalytic activity of CO_2 reduction. **(b)** CO selectivity. **(c)** Stability tests of CO_2 reduction of Ag-TiO_2@SiO_2. **(d)** Photocatalytic CO_2 reduction performance under different conditions. **(e)** CO evolution of the $^{13}CO_2$ isotope-labeled experiment.

To gain insight into the reaction pathway, in situ diffuse reflectance infrared Fourier transform spectroscopy (DRIFTS) was employed to monitor the intermediate species formed during the CO_2 reduction process [32]. As depicted in Figure 4a, upon irradiation, characteristic peaks emerged at 1706 cm^{-1} (carbonyl stretch $v(C=O)$ in carboxylic acids), 1550 cm^{-1} ($v_{as}(OCO)$, the antisymmetric telescopic vibration of OCO), 1409 cm^{-1} ($v_s(COO^-)$, the symmetrical stretching vibration of COO^-), and 1253 cm^{-1} ($v(C-OH)$, the stretching vibration of carboxylic acid hydroxyl group) [22,33]. The presence of these signals confirms that *COOH is a key intermediate in the CO_2 reduction pathway. Additionally, a weak peak at 2160 cm^{-1} was identified as adsorbed *CO [34]. Coupled with the fact that CO is the major gas product, a plausible reaction pathway can be inferred that CO_2 is activated and hydrogenated to form the *COOH intermediate, which then undergoes dehydration to yield *CO, followed by rapid desorption as gaseous CO. Based on the above results and discussions, a mechanism for the photocatalytic CO_2 reduction over the porous SiO_2-coated Ag-TiO_2 is proposed schematically in Figure 4b. Under light irradiation, TiO_2 generates electron-hole pairs. Given that the work function of Ag (4.26 eV) is higher than that of TiO_2 (4.20 eV), photogenerated electrons in TiO_2 spontaneously transfer to the Ag nanoparticles upon light irradiation, where they participate in reduction reactions. Concurrently, the photogenerated holes remain on TiO_2 and are involved in oxidation reactions, which predominantly occur at oxygen sites [26,35]. The key innovation lies in the porous SiO_2 shell, which constructs a localized hydrophobic microenvironment. The pore channels preferentially allow the diffusion of gaseous CO_2 molecules to the Ag active sites while effectively hindering the access of water molecules. This selective regulation of reactant supply enriches the local concentration of CO_2 around the active sites, thereby drastically suppressing the competition from the HER and ultimately leading to the high selectivity for CO production.
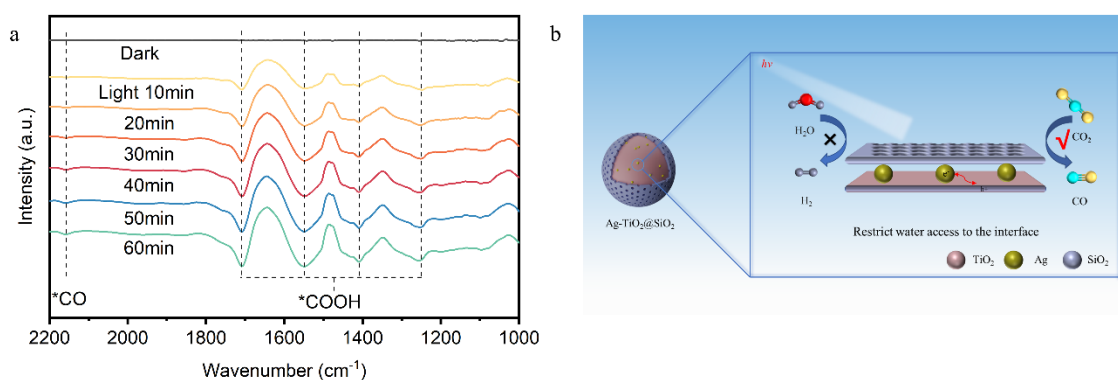

Figure 4. (**a**) In situ IR spectra of Ag-TiO_2@SiO_2. (**b**) The mechanism of CO_2 reduction on Ag-TiO_2@SiO_2.

4. Conclusions

In summary, we have developed a porous SiO_2-encapsulated Ag-TiO_2 photocatalyst that achieves 100% selectivity toward CO in the photocatalytic CO_2 reduction reaction without the use of any sacrificial agent. The remarkable enhancement in selectivity is attributed to the core-shell structure, in which the SiO_2 shell acts as a molecular sieve that preferentially permits the diffusion of CO_2 to the active sites while effectively restricting the access of water molecules to the catalytic interface. This work underscores the critical role of interfacial microenvironment engineering in regulating mass transport and suppressing competing reactions in three-phase photocatalytic systems. We believe this SiO_2 encapsulation strategy offers a versatile and scalable pathway for designing highly selective photocatalysts, and it may inspire further exploration of core-shell architectures for efficient solar fuel production and other gas-involved photocatalytic processes.

Author Contributions: M.J. conceived and designed the experiments. J.L. performed the catalyst preparation, characterization, and wrote the manuscript. Y.L., contributed to the HRTEM characterizations. Y.W. and Q.G. performed the catalytic tests. Z.G., Y.R., Y.Z., and Q.W. participated in the catalyst preparation and data analysis. The manuscript was written through the contributions of all authors. All authors have read and agreed to the published version of the manuscript.

Data Availability Statement: The authors confirm that the data supporting the findings of this study are available within the article and its supplementary materials.

Conflicts of Interest: The authors declare no conflict of interest.

Use of AI and AI-assisted Technologies: No AI tools were utilized for this paper.

References

1. Gao, W.; Liang, S.; Wang, R.; Jiang, Q.; Zhang, Y.; Zheng, Q.; Xie, B.; Toe, C.Y.; Zhu, X.; Wang, J.; et al. Industrial carbon dioxide capture and utilization: state of the art and future challenges. *Chem. Soc. Rev.* **2020**, *49*, 8584–8686.

2. Das, S.; Pérez-Ramírez, J.; Gong, J.L.; Dewangan, N.; Hidajat, K.; Gates, B.C.; Kawi, S. Core–shell structured catalysts for thermocatalytic, photocatalytic, and electrocatalytic conversion of CO_2. *Chem. Soc. Rev.* **2020**, *49*, 2937–3004.

3. Xie, Z.K.; Xu, S.J.; Li, L.H.; Gong, S.H.; Wu, X.J.; Xu, D.B.; Mao, B.D.; Zhou, T.; Chen, M.; Wang, X.; et al. Well-defined diatomic catalysis for photosynthesis of C_2H_4 from CO_2. *Nat. Commun.* **2024**, *15*, 2422.

4. Choi, C.; Kwon, S.; Cheng, T.; Xu, M.J.; Tieu, P.; Lee, C.; Cai, J.; Lee, H.M.; Pan, X.Q.; Duan, X.F.; et al. Highly active and stable stepped Cu surface for enhanced electrochemical CO_2 reduction to C_2H_4. *Nat. Catal.* **2020**, *3*, 804–812.

5. Li, X.; Sun, Y.; Xu, J.; Shao, Y.; Wu, J.; Xu, X.; Pan, Y.; Ju, H.; Zhu, J.; Xie, Y. Selective visible-light-driven photocatalytic CO_2 reduction to CH_4 mediated by atomically thin $CuIn_5S_8$ layers *Nat. Energy* **2019**, *4*, 690–699.

6. Fang, S.; Rahaman, M.; Bharti, J.; Reisner, E.; Robert, M.; Ozin, G.A.; Hu, Y.H. Photocatalytic CO_2 reduction. *Nat. Rev. Methods Primers* **2023**, *3*, 61.

7. Kong, T.T.; Low, J.X.; Xiong, Y.J. Catalyst: How Material Chemistry Enables Solar-Driven CO_2 Conversion. *Chem* **2020**, *6*, 1035–1038.

8. Zhou, Q.X.; Guo, Y.; Zhu, Y.F. Reticular copper dual sites embedded with semiconductor particles for selective CO_2-to-C_2H_4 photoreduction. *Nat. Catal.* **2025**, *8*, 728–739.

9. Li, J.; Chen, G.; Zhu, Y.; Liang, Z.; Pei, A.; Wu, C.-L.; Wang, H.; Lee, H.R.; Liu, K.; Chu, S.; et al. Efficient electrocatalytic CO_2 reduction on a three-phase interface. *Nat. Catal.* **2018**, *1*, 592–600.

10. Jiang, Z.F.; Sun, H.L.; Wang, T.Q.; Wang, B.; Wei, W.; Li, H.M.; Yuan, S.Q.; An, T.C.; Zhao, H.J.; Yu, J.G.; et al. Nature-based catalyst for visible-light-driven photocatalytic CO_2 reduction. *Energy Environ. Sci.* **2018**, *11*, 2382–2389.

11. Zhang, Y.Z.; Xia, B.Q.; Ran, J.R.; Davey, K.; Qiao, S.Z. Atomic-Level Reactive Sites for Semiconductor-Based Photocatalytic CO_2 Reduction. *Adv. Energy Mater.* **2020**, *10*, 1903879.

12. Wei, Y.; Mao, Z.J.; Jiang, T.W.; Li, H.; Ma, X.Y.; Zhan, C.; Cai, W.B. Uncovering Photoelectronic and Photothermal Effects in Plasmon-Mediated Electrocatalytic CO_2 Reduction. *Angew. Chem. Int. Ed.* **2024**, *63*, e202317740.

13. Mohata, S.; Das, R.; Koner, K.; Riyaz, M.; Das, K.; Chakraborty, S.; Ogaeri, Y.; Nishiyama, Y.; Peter, S.C.; Banerjee, R. Selective Metal-Free CO_2 Photoreduction in Water Using Porous Nanostructures with Internal Molecular Free Volume *J. Am. Chem. Soc.* **2023**, *145*, 23802–23813.

14. Wu, X.Y.; Li, Y.; Zhang, G.K.; Chen, H.; Li, J.; Wang, K.; Pan, Y.; Zhao, Y.; Sun, Y.F.; Xie, Y. Photocatalytic CO_2 Conversion of $M_{0.33}WO_3$ Directly from the Air with High Selectivity: Insight into Full Spectrum-Induced Reaction Mechanism *J. Am. Chem. Soc.* **2019**, *141*, 5267–5274.

15. Su, H.; Yin, H.; Orbell, W.; Li, Y.; Wang, G.; Wang, Y.; Mori, K.; Chen, Z.; Li, H.; Yamashita, H.; et al. Asymmetric Triple-Atom Sites Combined with Oxygen Vacancy for Selective Photocatalytic Conversion of CO_2 to Propionic Acid *Angew. Chem. Int. Ed.* **2025**, *64*, e202425446.

16. Ren, Y.; Si, Y.; Du, M.; You, C.; Zhang, C.; Zhu, Y.-H.; Sun, Z.; Huang, K.; Liu, M.; Duan, L.; et al. Photothermal Synergistic Effect Induces Bimetallic Cooperation to Modulate Product Selectivity of CO_2 Reduction on Different CeO_2 Crystal Facets. *Angew. Chem. Int. Ed.* **2024**, *63*, e202410474.

17. Wang, J.; Zhang, H.; Nian, Y.; Chen, Y.; Cheng, H.; Yang, C.; Han, Y.; Tan, X.; Ye, J.; Yu, T. Disruption Symmetric Crystal Structure Favoring Photocatalytic CO_2 Reduction: Reduced *COOH Formation Energy Barrier on Al Doped CuS/TiO_2. *Adv. Funct. Mater.* **2024**, *34*, 2406549.

18. Ma, Y.; Jiang, Q.; Li, X.; Yu, H.; Han, X.; Liu, Y.; Li, Q.; Lv, K.; Hu, J. Heterojunction constructed from ZIF-8-on-MIL-68(Ga) precursor for photocatalytic CO_2 reduction. *Chem. Commun.* **2025**, *61*, 6831.

19. Kim, C.; Cho, K.M.; Al-Saggaf, A.; Gereige, I.; Jung, H.T. Z-scheme Photocatalytic CO_2 Conversion on Three-Dimensional $BiVO_4$/Carbon-Coated Cu_2O Nanowire Arrays under Visible Light. *ACS Catal.* **2018**, *8*, 4170–4177.

20. Guo, F.; Li, R.-X.; Yang, S.; Zhang, X.-Y.; Yu, H.; Urban, J.J.; Sun, W.-Y. Designing heteroatom-codoped iron metal–organic framework for promotional photoreduction of carbon dioxide to ethylene. *Angew. Chem. Int. Ed.* **2023**, *62*, e202216232.

21. Hu, S.; Qiao, P.; Yi, X.; Lei, Y.; Hu, H.; Ye, J.; Wang, D. Selective Photocatalytic Reduction of CO_2 to CO Mediated by Silver Single Atoms Anchored on Tubular Carbon Nitride *Angew. Chem. Int. Ed.* **2023**, *62*, e202304585.

22. Li, A.; Cao, Q.; Zhou, G.; Schmidt, B.V.K.J.; Zhu, W.; Yuan, X.; Huo, H.; Gong, J.; Antonietti, M. Three-Phase Photocatalysis for the Enhanced Selectivity and Activity of CO_2 Reduction on a Hydrophobic Surface. *Angew. Chem. Int. Ed.* **2019**, *58*, 14549–14555.

23. Wang, R.A.; Zhang, M.J.; Zhang, S.L.; Zheng, J.Z.; Zeng, Y.Q.; Yang, Y.; Ding, J.; Wu, X.; Zhong, Q. Simultaneous Photocatalytic CO2 Reduction and H2O Oxidation Under Non-Sacrificial Ambient Conditions.*ACS Nano* **2023**, *17*, 24363–24373.

24. Wang, Y.; Huang, N.-Y.; Shen, J.-Q.; Liao, P.-Q.; Chen, X.-M.; Zhang, J.-P. Hydroxide Ligands Cooperate with Catalytic Centers in Metal–Organic Frameworks for Efficient Photocatalytic CO_2 Reduction. *J. Am. Chem. Soc.* **2018**, *140*, 38–41.

25. Robert, M.; Zhang, J.-H.; Ge, Z.-M.; Zhong, D.-C.; Zuo, J.-L.; Lu, T.-B. Self-Photosensitizing Cobalt Complexes for Photocatalytic CO_2 Reduction Coupled with CH_3OH Oxidation. *Angew. Chem. Int. Ed.* **2025**, *64*, e202506060.

26. Yu, Y.Y.; He, Y.; Yan, P.; Wang, S.Y.; Dong, F. Boosted C-C coupling with Cu-Ag alloy sub-nanoclusters for CO_2-to-C_2H_4 photosynthesis. *Proc. Natl. Acad. Sci. USA* **2023**, *120*, e2307320120.

27. Deng, Y.; Qi, D.; Deng, C.; Zhang, X.; Zhao, D. Superparamagnetic High-Magnetization Microspheres with an $Fe_3O_4@SiO_2$ Core and Perpendicularly Aligned Mesoporous SiO_2 Shell for Removal of Microcystins. *J. Am. Chem. Soc.* **2008**, *130*, 28–29.

28. Huang, H.N.; Shi, R.; Li, Z.H.; Zhao, J.Q.; Su, C.L.; Zhang, T.R. Triphase Photocatalytic CO_2 Reduction over Silver-Decorated Titanium Oxide at a Gas–Water Boundary. *Angew. Chem. Int. Ed.* **2022**, *61*, e202200802.

29. Yin, C.; Li, X.; Sun, S.; Wei, X.; Tong, Q.; Tan, W.; Wang, X.; Peng, B.; Wan, H.; Dong, L. High photocatalytic performance over ultrathin 2D TiO_2 for CO_2 reduction to alcohols. *Chem. Commun.* **2024**, *60*, 3531–3534.

30. Xia, P.F.; Antonietti, M.; Zhu, B.C.; Heil, T.; Yu, J.G.; Cao, S.W. Designing Defective Crystalline Carbon Nitride to Enable Selective CO_2 Photoreduction in the Gas Phase. *Adv. Funct. Mater.* 2019, **29**,1900093.

31. Jiang, M.; Gao, Y.L.; Wang, Z.Y.; Ding, Z.X. Photocatalytic CO_2 reduction promoted by a $CuCo_2O_4$ cocatalyst with homogeneous and heterogeneous light harvesters. *Appl. Catal. B* **2016**, *198*, 180–188.

32. Kattel, S.; Yu, W.T.; Yang, X.F.; Yan, B.H.; Huang, Y.Q.; Wan, W.M.; Liu, P.; Chen, J.G.G. CO_2 Hydrogenation over Oxide-Supported PtCo Catalysts: The Role of the Oxide Support in Determining the Product Selectivity. *Angew. Chem. Int. Ed.* **2016**, *55*, 7968–7973.

33. Zhao, Z.J.; Mu, R.T.; Wang, X.H.; Gong, J.L. Fast prediction of CO binding energy via the local structure effect on PtCu alloy surfaces. *Langmuir* **2017**, *33*, 8700–8706.

34. Su, B.; Wang, S.; Xing, W.; Liu, K.; Hung, S.-F.; Chen, X.; Fang, Y.; Zhang, G.; Zhang, H.; Wang, X. Synergistic Ru Species on Poly(heptazine imide) Enabling Efficient Photocatalytic CO_2 Reduction with H_2O beyond 800 nm. *Angew. Chem. Int. Ed.* **2025**, *64*, e202505453.

35. Kaushik, T.; Ghosh, S.; Dolkar, T.; Biswas, R.; Dutta, A. Noble Metal Plasmon–Molecular Catalyst Hybrids for Renewable Energy Relevant Small Molecule Activation. *ACS Nanosci. Au* **2024**, *4*, 273–289.